The thermal structure of the lithosphere from shear wave velocities

Keith Priestley, Dan McKenzie *

Department of Earth Sciences, Bullard Labs Madingley Road, Cambridge CB3 0EZ, U.K.

Abstract

The low shear wave velocities V_s observed beneath spreading ridges and in the low velocity zone beneath plates are commonly attributed to the presence of melt. But geochemical observations suggest that the amount of melt present in those parts of the mantle that are melting is about 0.1%, which is too small to produce a major decrease in V_s. Furthermore laboratory measurements of V_s at seismic frequencies, $1–10^{-2}$ Hz, show that V_s is more strongly affected by temperature than by the presence of a few percentage of melt. It is, however, not straightforward to use laboratory experiments to relate V_s to the temperature T because the grain size of most laboratory experiments is 100–1000 times smaller than that of the mantle. We combine thermal models of the Pacific lithosphere and pressure and temperature estimates from mantle nodules brought up by kimberlites with three dimensional models of V_s from surface wave tomography to obtain an empirical relation for $V_s(P, T)$, where P is the pressure. This expression is then used to convert regional variations of V_s as a function of depth to lithospheric thickness. The accuracy of the resulting maps is tested by comparison with the location of diamond-bearing kimberlites, which are in most places restricted to regions where the lower part of the lithosphere is in the diamond stability field.
© 2006 Elsevier B.V. All rights reserved.

1. Introduction

The thickness of the lithosphere, the cold boundary layer near the Earth's surface, controls the heat loss and tectonics of oceans and continents. When Gutenberg (see [1, pp. 76–89]) discovered the low velocity zone in the upper mantle, he pointed out that its position corresponded to the closest approach of the geotherm to the melting temperature. The thickness of the high velocity lid above the low velocity layer is often taken to be the same as the lithospheric thickness. But it is not obvious that the two are the same. 'Lithosphere' is a geodynamical concept: it is the part of the mantle that

forms rigid plates, within which heat is transported by conduction. Neither property has a direct influence on seismic velocities. Therefore the correspondence between seismic velocities and the long term mechanical properties of the mantle is unlikely to be simple, and is the principal concern of this paper. An obvious method of relating the two is through the temperature, which affects the seismic velocity. The base of the lithosphere must correspond to the depth at which heat transport changes from conduction to advection. If seismic velocity profiles can be converted to temperature profiles, the base of the lithosphere should be marked by a rapid decrease in the temperature gradient with depth.

The association between low seismic velocity and high temperature has lead to a number of proposals that

* Corresponding author. Tel.: +44 1223337191.
 E-mail address: mckenzie@esc.cam.ac.uk (D. McKenzie).

small amounts of partial melt, distributed in thin cracks, are responsible for reducing the seismic velocity in the mantle [2–4]. Such discussions have principally been concerned with the macroscopic behaviour of a two phase continuum, where both the solid and melt are described as continuous media. The presence of melt can affect seismic velocities in two ways; by macroscopic movement through channels, a process which is sometimes referred to as 'melt squirt', and by relaxing the shear stresses between grains. As Karato [5] pointed out, the second process does not require a macroscopic melt phase.

Probably the best constraint on the amount of melt that is likely to be present in those parts of the mantle containing partial melt comes from measurements of activity ratios of (^{230}Th/^{238}U), (^{231}Pa/^{235}U) and (^{226}Ra/^{230}Th) in young magnesium-rich basalts from ridges and oceanic islands, most of which are greater than 1. Differences in the chemical behaviour of the parent isotopes ^{238}U, ^{235}U and ^{230}Th and their daughter products ^{230}Th, ^{231}Pa and ^{226}Ra, cause the parents to be preferentially partitioned into the solid residue during melting. Since all the elements involved have small partition coefficients between melt and solid, these observations constrain the amount of melt present during melting to be about 0.1% (see [6,7]). Both theoretical studies of the macroscopic behaviour of two phase materials [3] and experimental studies of the influence of melt on V_s [8] suggest that such small melt fractions will have little effect on the shear modulus. It is therefore unlikely that the observed variations in V_s within the mantle at a particular depth are caused by melt squirt.

Most laboratory measurements of V_s have been carried out at MHz frequencies. Recently two groups [9,10] have extended such measurements to seismic frequencies, of a few millihertz. At these frequencies large decreases in V_s occur at temperatures that are 100–200 °C below the melting point. Gribb and Cooper [9] argue that the cause of this behaviour is the relaxation of grain boundary stresses, caused by diffusion. The regular arrangement of atoms in the crystals becomes disordered on grain boundaries. Whether such disordered regions are described as molten is a matter of semantics. At high temperatures the atoms in such regions become mobile, and the shear stresses across grain boundaries may then be relaxed by grain boundary diffusion. Whether such relaxation will occur during the passage of a seismic wave depends on whether the time scale for diffusion is short or long compared with the period of the seismic wave. The characteristic relaxation time of shear stresses on grain boundaries will decrease

rapidly with increasing temperature, and the shear wave velocity will therefore depend strongly on the frequency of the seismic wave. However, the disordered material on the grain boundary does not form a macroscopically distinct molten phase at temperatures below the macroscopic solidus.

Priestley and McKenzie [11] used Gribb and Cooper's [9] experimental observations to argue that the region with low V_s velocity beneath the lithosphere simply results from its high temperature, and does not require the presence of a macroscopic melt phase. They showed that the top of the seismic low velocity zone beneath southern Africa occurs at the base of the lithosphere, where the mechanism of heat transport changes from conduction to advection with increasing depth and the temperature gradient decreases. However, they did not attempt to parameterise the relationship between V_s and temperature.

Faul and Jackson [12] have recently taken a phenomenological approach to parameterising the dependence of V_s on temperature T, pressure P, and grain size d. They modified expressions that Kanamori and Anderson [13] and Anderson and Minster [14] proposed to describe the behaviour of both V_s and the attenuation Q. The expressions they use are consistent with the Kramers–Kronig relations (see [15], pp. 206–216), but their functional form is not derived from a microscopic model of stress transmission in a polycrystalline solid. Faul and Jackson's expressions are complicated, and contain more than nine adjustable constants, which they determined by fitting their experimental observations. It is unclear whether their expressions will give accurate values of V_s when they are used to extrapolate outside the experimental range of temperature, pressure and grain size, rather than for interpolation. The grain size dependence is especially problematic, since most experiments have been carried out using grain sizes of less than 25 μm, whereas the grain size of the upper mantle likely to be at least 1000 μm.

It is therefore important to test the accuracy of Faul and Jackson's [12] expressions before they are applied to the mantle. Several tests are available. Jackson et al. [16] carried out a careful study of the effect of melt on V_s, and argued that all of Gribb and Cooper's [9] charges contained melt. Gribb and Cooper used higher temperatures than Jackson et al., and found larger decreases in the shear modulus. Gribb and Cooper [8] argue that this behaviour is independent of the presence or absence of a macroscopic melt phase. If they are correct, their measurements can be used to test the accuracy of Faul and Jackson's [12] parameterisation. Geological and

geophysical estimates of mantle temperatures from regions where V_s is known can also be used for this purpose. Section 3 discusses the results of these tests, which demonstrate that Faul and Jackson's expressions can underestimate $|(\partial V_s / \partial T)_P|$ when the temperature approaches the melting temperature.

An alternative approach, which we use here, is to use geophysical and petrological models of the lithosphere to construct an empirical parameterisation of V_s. The functional form of the parameterisation is based on the idea that anaelastic behaviour at temperatures approaching the melting temperature depends on some process with an activation energy. Our expression has no explicit dependence on grain size or seismic frequency, and therefore cannot be used to relate V_s to Q. We then use temperature profiles calculated from $V_s(z)$ to map the lithospheric thickness of the continents. The study that most closely resembles ours is that of Shapiro et al. [17], who used the phase and group velocities of fundamental mode Rayleigh waves across the Canadian Shield to map lithospheric thickness. We use the phase velocities of the first four higher modes, as well as that of the fundamental mode, in order to improve both vertical and lateral resolution at the base of the lithosphere.

2. Data and analysis

We constructed 3D upper mantle models for the various regions discussed in this paper using the two-stage procedure previously employed in a number of regional scale surface wave tomography studies [18,19]. In the first stage we use the automated version [20] of Cara and Lévêque's [21] waveform inversion technique to model each multi-mode Rayleigh waveform in the 50–160 s period range to determine the path-average mantle SV-wave speed structure. In the second stage we combined the 1D velocity models in a tomographic inversion [22,23] to obtain a 3D model of the SV-wave speed structure and the azimuthal anisotropy as a function of depth. Such models give a clearer indication of the properties at depth than do group and phase velocity maps, which represent weighted averages of the earth structure over a frequency-dependent depth interval. Debayle and Kennett [18] provide details of the analysis procedure.

There are two assumptions inherent in our analysis—that the observed surface waveform can be represented by multi-mode surface waves propagating independently along great circle paths. These assumptions are valid for a smoothly varying medium without strong lateral velocity gradients [24]. Kennett [25] examined the validity of the great circle approximation for surface wave propagation at regional continental scale and concluded that the assumption was valid at longer periods ($>$50 s) where surface waves cross major structural boundaries such as the continent–ocean transition. Ritzwoller et al. [26] examined the effects of off-great circle propagation and found that for short path lengths ($\sim$5000 km), the great circle assumption was adequate but led to increasing bias in the inverted model as path length increased. Marquering et al. [27] examined the effect of mode coupling and found that when a large number ($\sim$20) of short period (to 10 s) modes were included and mode-coupling was neglected, the shallow parts of the inversion model which are sampled by the fundamental mode and the first few
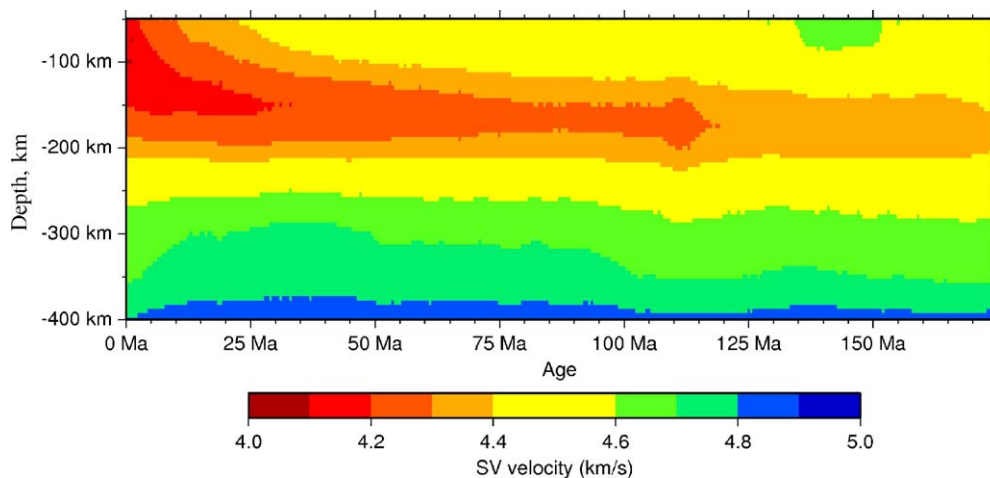

Fig. 1. Shear wave velocity beneath the Pacific Ocean, obtained from surface wave tomography using the fundamental and first four higher modes, averaged as a function of age from Mueller et al. [29].

higher modes accurately represented the true model, but the deeper parts (~400 km) of the inversion model could contain artifacts. We therefore restricted our analysis to the fundamental and first four higher Rayleigh modes in the 50–160 s period band, and attempted to restrict our analysis to events with relatively short paths compared to those used in global studies, while maintaining good azimuthal coverage. However, we did not use paths shorter than about 1000 km, because shorter paths do

not produce enough dispersion between different modes to allow their phase velocities to be accurately determined. The availability of higher mode phase velocities produces a striking improvement in the vertical resolution (see for instance Dahlen and Tromp [15], pp. 448–9).

The lateral smoothness of the tomographic model is constrained by a Gaussian a priori covariance function L_{corr}, the horizontal distance over which neighboring
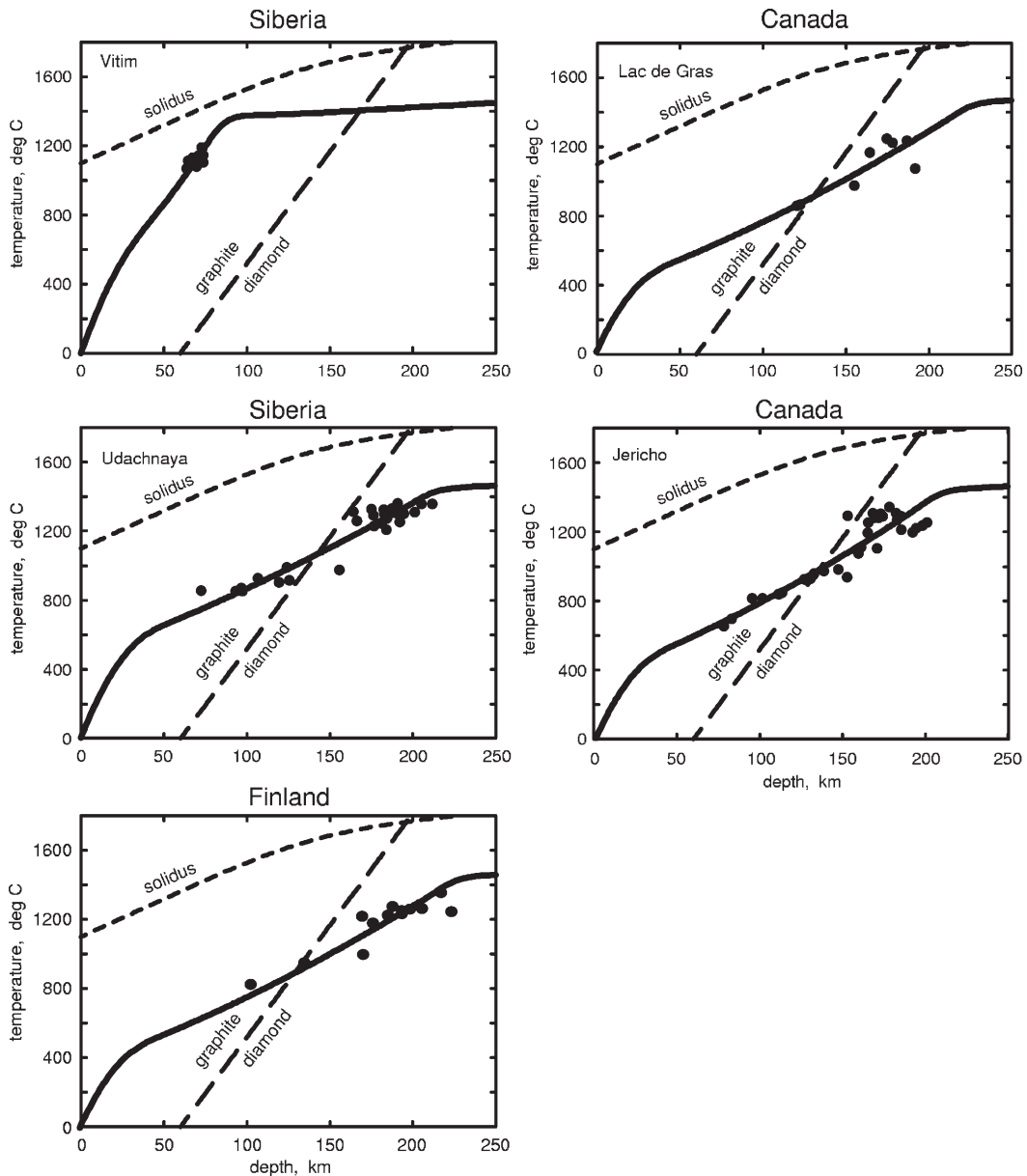

Fig. 2. The points show depth and temperature estimates from mineral compositions of nodules from four diamond-bearing kimberlite pipes, from Lac de Gras, Jericho, Udachnaya, and Finland, and from an alkali basalt from Vitim (see Table 1 for sources), calculated from Brey and Kohler's [31] expressions. These have been fitted to geotherms using the methods outlined in McKenzie et al. [32] to estimate the lithospheric thicknesses. The diamond-graphite phase boundary is from Kennedy and Kennedy [55].

points correlate. For the Pacific we chose $L_{corr} = 800$ km, thus favouring a smooth model considering our ray density and shortest wavelength used (about 200 km at 50 s period). Sieminski et al. [28] show that using a dense coverage of relatively short paths and assuming ray theory, it is possible to detect heterogeneity with length scales smaller than the wavelength of the data set.

The data used to build the Pacific tomographic model consists of 69,005 vertical component, long-period Rayleigh waveforms from 10,793 earthquakes occurring between 1977 and 2003 recorded at 335 seismic stations within or on the periphery of the Pacific Basin. While we sought to minimize the number of long propagation paths, longer paths—particularly in the north Pacific—were required to maintain good path coverage. The path density for our data is heterogeneous. To provide more uniform coverage we clustered the model by computing summary models for those paths with end points lying within a 400 km radius of each other, after computing the 1D SV-velocity path-average models. This approach gives a smoother distribution of 9606 1D models and provides error estimates for the input in the second stage of the analysis.

Temperature estimates from within the lithosphere are available from two sources: from thermal models of oceanic plates, and from pressure and temperature estimates from nodules brought to the surface by kimberlites and alkali basalts. The temperature structure of oceanic lithosphere depends principally on its age. We obtained that of the Pacific by smoothing the sea floor-age map [29], suppressing wavelengths less than 1000 km and interpolated the smoothed sea floor-age map to the same 2×2 grid as the seismic model for the Pacific. We then stacked points of common age (± 1 Ma) which were away from obvious sea floor anomalies, to give the velocity vs. age shown in Fig. 1. To obtain temperature estimates from the continental lithosphere we used the composition of minerals from nodules transported by kimberlites and alkali basalts. We used the five geotherms obtained from such nodule suites to constrain $V_s(z, \Theta)$, which are illustrated in Fig. 2 and listed in Table 1. Estimates of depth and pressure from nodules were first obtained using Finnerty and Boyd's [30] and Brey and Kohler's [31] expressions. Geotherms were then fitted to the pressure and temperature estimates from Brey and Kohler's estimates using the approach outlined in McKenzie et al. [32]. Corresponding profiles of $V_s(z)$ were obtained from surface wave tomography. The nodule suite from Vitim was used because the estimated thickness of the lithosphere is smaller than that from most shields. The others have thicker lithosphere, and were chosen

Table 1
Lithospheric thickness estimates

	N latitude	E longitude	V_s (km)	F. and B. [30] (km)	B. and K. [31] (km)
Somerset Island [43,44]	73.44	−90.82	204	179	159
Jericho [45]	66	−111.49	218	217	201
Lac de Gras [46]	64	−110	224	222	218
Kirkland Lake [47]	48.1	−79.8	219	210	215
Finland [48]	62.93	28.08	232	226	221
Udachnaya [49]	66.42	112.85	188	231	205
Obnazhennaya [50]	70.48	121.3	175	166	171
Vitim [51]	54.02	113.58	(104)	102	88
India [52]	15	77.3	(134)	180	164
Chyulu [53]	−2.3	37.83	(107)	–	91
Marsabit [53]	2.33	37.98	(106)	–	88
Labiat [54]	−4.57	35.43	–	–	143

V_s—F. and B. mean=0 km, rms=19 km V_s—B. and K. mean=12 km, rms=17 km both calculated using only the first 7 entries in the table. Near Labiat the calculated lithospheric thickness changes by about 200 km (see Fig. 10a).

because the pressures estimated from the nodules from a single kimberlite pipe cover a large depth range.

The oceanic lithosphere at depths greater than about 50 km consists of garnet peridotite, from which only a few percentage of melt has been removed. In contrast, the upper part of the mantle beneath shields consists of harzburgite (see [33]), formed from peridotite by the removal of 20–25% melt, which therefore has a different composition from that of the oceanic lithosphere. Clearly a single empirical expression can only be used to calculate $V_s(z, \Theta)$ if the effects of this difference in composition are small. The effect of melt removal on the density, V_s, $mg\#$ and mode is shown in Fig. 3. The curves were calculated by removing melt from the fertile mantle composition of McKenzie and O'Nions [34], using the parameterisation of McKenzie and Bickle [35] and a melting depth of 85 km. The mode of the residue and its density were obtained from its composition using the mineral compositions listed in Table 1 of McKenzie and O'Nions. The shear wave velocity was then calculated from the Voigt–Reuss–Hill average of the V_s velocity of the phases [36, Appendix C]. The densities and velocities in Fig. 3 are calculated at a depth of 70 km and a temperature of 500 °C. The behaviour agrees with that found by Jordan [37]. Melt removal has a minor effect on V_s, even when 20–25% melt is removed, but has a large effect on the density of
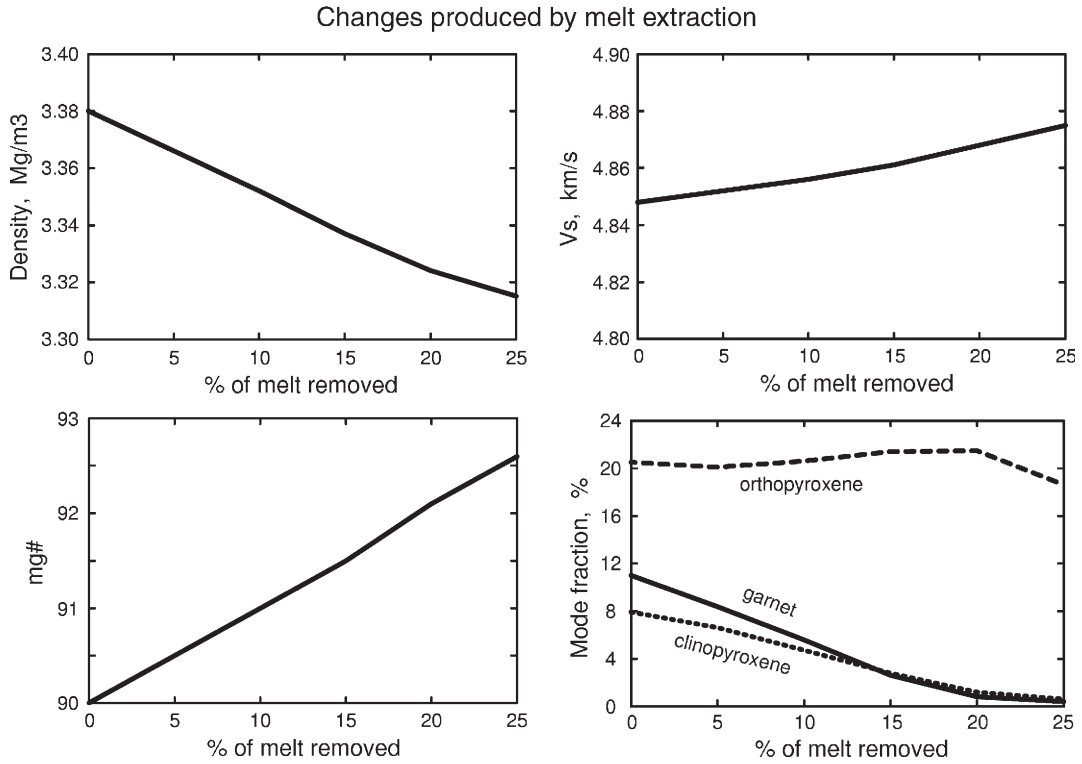
Changes produced by melt extraction

Fig. 3. Changes in density, V_s, $mg\#$, and mineral mode resulting from the extraction of melt from a fertile garnet peridotite (see text). The variation in density in (a) is the same as that produced by a temperature increase of about 500 °C with a thermal expansion coeffcient of $4 \times 10^{-5}/$ °C. The range in V_s is equivalent to a change in temperature of 96 °C when the temperature is less than about 1100°.

the residue. The velocity of the residual harzburgite is only about 0.03 km/s greater than that of undepleted peridotite.

3. Parameterisation of V_s

Fig. 4 compares Faul and Jackson's [12] parameterisation with Jackson et al.'s [16] and Gribb and Cooper's [9] measurements for material with a grain size of 3 μm at two different frequencies, 3.3 and 100 s. As expected, the results from Faul and Jackson's [12] expressions agree well with Jackson et al.'s [16] results at both frequencies, which were used in their parameterisation. They also agree well with Gribb and Cooper's [9] measurements at 100 s, but not with those at 3.3 s, where the observed velocities are substantially less than those predicted. Gribb and Cooper [8] argue that their measured velocities are not affected by the presence of melt, but Jackson et al. [16] disagree.

Another test of Faul and Jackson's parameterisation exploits the thermal models of the oceanic lithosphere. Fig. 1 shows the average variation of V_s with depth z and age t for the Pacific, obtained from Rayleigh wave tomography using the fundamental and first four higher

modes. These observations can be converted to $V_s(z, \Theta)$, where Θ is the temperature in °C, using a thermal model of a cooling plate. That used here has a plate thickness of
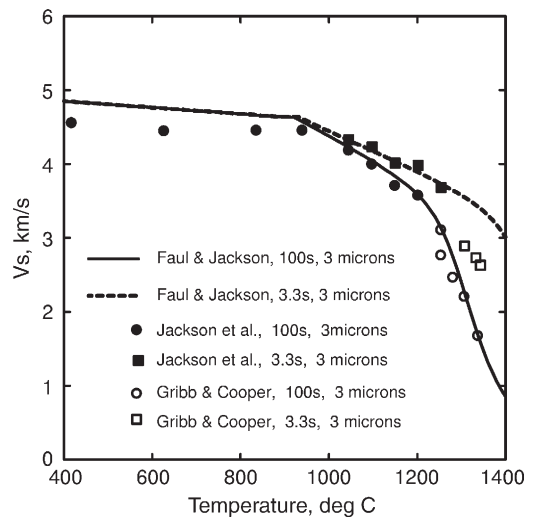

Fig. 4. Laboratory measurements of V_s, calculated from $V_s^2 = \mu / \rho$ with $\rho = 3.3 \times 10^3$ kg/m^3, from Jackson et al. [16] and from Gribb and Cooper [9] for two different periods. The lines are calculated from Faul and Jackson's [12] expressions.

106 km, and takes account of the variation of thermal conductivity, thermal expansion and specific heat with temperature [32]. Fig. 5a shows $V_s(\Theta)$ calculated in this way for two depths, 50 and 75 km, together with the region corresponding to one standard deviation of V_s for the 50 km curve, and that calculated from Faul and Jackson's [12] expressions at a depth of 50 km and a grain size of 1 mm. The corresponding curve for 100 km was not used, because the calculated temperature at this depth is principally controlled by the choice of plate thickness. For instance, if the plate thickness is taken to be 100 km, rather than 106 km, which is within the observed uncertainty, the calculated temperature is constant. Faul and Jackson's expression has a larger value of V_s than that observed at temperatures of less than about 1300 °C, and a smaller value of $|(\partial V_s/\partial T)_P|$

Fig. 5. (a) V_s as a function of temperature, obtained from Fig. 1 using the thermal model of McKenzie et al. [32] for two depths, 50 and 75 km. The shaded region shows one standard deviation of the velocity at 50 km, calculated from the age-binned data used in Fig. 1. The standard deviations at 75 km is similar. The dashed blue line shows $V_s(z,\Theta)$ from Faul and Jackson's [12] expressions for a grain size of 1 mm, and the dashed green line shows that from Shapiro and Ritzwoller's [39] expressions (A11) and (A13), calculated using $A = 0.196$, rather than the value they give (Ritzwoller, personal communication 2005). (b) Comparison of the parameterisation derived here with the Pacific data.

at higher temperatures. Fig. 4 shows that Gribb and Cooper's [9] measurements at a period of 3.3 s also require a larger decrease in V_s at high temperature than that given by Faul and Jackson's expressions. The curve calculated using Goes et al.'s [38] expression and Shapiro and Ritzwoller's [39, and personal communication] constants (Fig. 5a) is similar to that of Faul and Jackson, and also does not produce a good fit to the Pacific observations.

The observed behaviour of $V_s(z,\Theta)$ shown in Fig. 5a can be understood in terms of a simple model of a solid aggregate. At low temperatures the elastic behaviour is controlled by interatomic forces and no slip occurs between grains. With increasing pressure the density, and hence the elastic moduli and the seismic wave velocities, of the solid increase. Similarly with increasing temperature thermal expansion causes a decrease in density, elastic moduli and seismic velocities. As the temperature approaches the melting temperature, activated processes that relax the grain boundary stresses become important, reducing the shear modulus and increasing the anelastic effects. Laboratory experiments do not yet provide much information about the microscopic processes involved in the anelastic behaviour, though they presumably involve the movement of vacancies and interstitial atoms, either along the grain boundaries or through the crystals themselves. Fig. 5a shows how the observed values of V_s in the Pacific lithosphere are affected by these three effects, and suggests that a suitable parameterisation is
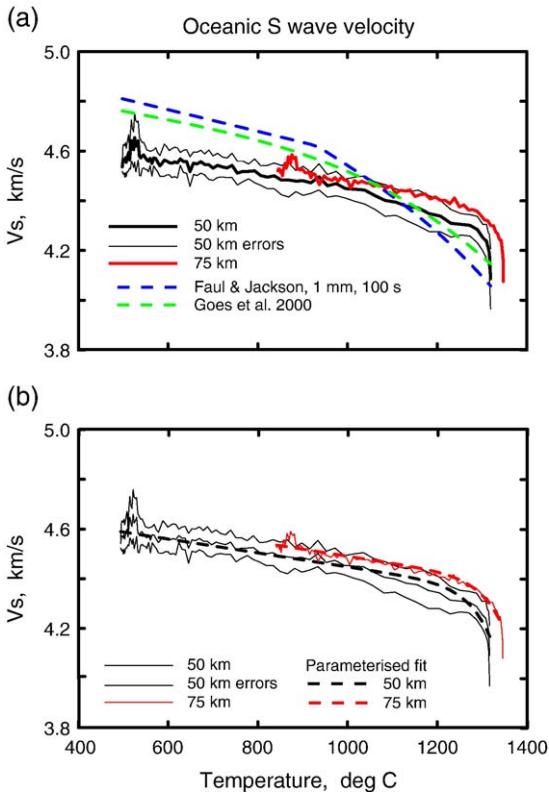
$$V_s = V_s(P, \Theta, a) \qquad (1)$$

where P is the pressure, Θ the temperature in °C and a is a variable describing the activation process

$$a = A'\exp{-(E + PV_a)/RT} \qquad (2)$$

where A' is a frequency factor, E the activation energy, V_a the activation volume and T is the temperature in Kelvin. The activated process responsible for the rapid decrease in V_s as the melting point is approached is presumably the same as that responsible for the corresponding decrease in Q. It is convenient to remove the nonactivated part of the pressure dependence of V_s by writing

$$V_s^\star = V_s/(1 + b_V(z-50)) \qquad (3)$$

where z is the depth in km and b_V is an empirical constant. Since the variation of V_s in the upper mantle is small, we expand $V_s^\star(a)$ using a Taylor series

$$V_s^\star(a) = V_s^\star(0) + \left(\frac{\partial V_s^\star}{\partial a}\right)_0 a \qquad (4)$$

and write

$$V_s^\star = m\Theta + c + A\exp{-(E + PV_a)/RT}. \qquad (5)$$

The six empirical constants were then determined by minimising H_1 where

$$H_1 = \frac{1}{2}\sum_{j=1}^{2}\left[\frac{1}{N_j}\sum_{i=1}^{N_j}\frac{(V_i^j(\text{obs})-V_i^j(\text{calc}))^2}{(\sigma_i^j)^2}\right]^{1/2} \qquad (6)$$

where $V_i^j(\text{obs})$, σ_i^j and $V_i^j(\text{calc})$ are the observed shear velocity, its standard deviation and the calculated velocity at depths of 50 km ($j=1$) and 75 km ($j=2$), respectively. The principal difficulty experienced with this approach was that b_V and V_a both control the pressure dependence of V_s and were not individually well determined. This ambiguity was resolved by using the five geotherms shown in Fig. 2. Velocity profiles V_i at the same locations at depth intervals of 25 km where first obtained from the velocity models, then the temperature at these depths calculated from the nodule geotherms. These values were then used to obtain H_2

$$H_2 = \left[\frac{1}{N}\sum_{i=1}^{N}(V_i(\text{obs})-V_i(\text{calc}))^2\right]^{1/2}. \qquad (7)$$

The parameters of the empirical expression were then obtained by minimising H where

$$H = 0.1H_1 + 0.9H_2. \qquad (8)$$

The factors 0.1 and 0.9 were chosen so that the misfits H_1 and H_2 were given approximately equal weight in the minimisation. The fits to the velocities from the oceanic lithosphere are shown in Fig. 5b, and those to the nodule data in Fig. 6. Both match the observations well at all depths. The best fit gave values of $H_1=0.399$ and $H_2=0.049$. Fig. 6 also shows a comparison of V_s from Faul and Jackson's expressions for a grain size of 1 mm. This grain size gives velocities that are too low at high temperatures, in the lower part of the lithosphere and in the asthenosphere. Faul and Jackson found the same behaviour and proposed that the grain size increases with depth. Fig. 6e shows the effect of increasing the grain size from 1 mm to 3 cm. Though the resulting values of V_s agree better with those observed, it is likely that the average grain size decreases, rather than increases, with increasing depth [33]. Harzburgite consists of two minerals, olivine, Mg_2SiO_4 and Fe_2SiO_4, and orthopyroxene, $MgSiO_3$ and $FeSiO_3$. Grain growth of both olivine and orthopyroxene can occur by diffusion of Mg^{2+}, Fe^{2+} and Si^{4+}

through both minerals. In contrast, clinopyroxene, containing Ca^{2+}, and garnet, containing Al^{3+}, are present in fertile mantle, and these elements cannot easily diffuse through olivine, which is the dominant mineral. Grain growth by diffusion is therefore likely to be faster in harzburgite than it is in garnet peridotite. Perhaps for this reason, the grain size in nodules tends to become smaller as their depth of origin increases and the mantle becomes more fertile [33]. The fertile mantle below the lithosphere is strongly sheared by plate motion, which is also likely to reduce the grain size.

The values of the constants obtained by fitting both the Pacific data and that from the nodules are

$$b_V = 3.84 \times 10^{-4}\ \text{km}^{-1},$$

$$m = -2.8 \times 10^{-4}\ \text{km s}^{-1}\ \text{\$C}^{-1},$$

$$c = 4.72\ \text{km s}^{-1}, \quad A = -1.8 \times 10^{13}\ \text{km s}^{-1},$$

$$E = 409\ \text{kJ mol}^{-1},$$

$$V_a = 10 \times 10^{-6}\ \text{m}^3\ \text{mol}^{-1}(\equiv 10\ \text{cm}^3\ \text{mol}^{-1}) \qquad (9)$$

$V_s(z,\Theta)$ can be obtained from Eqs. (3) and (5). To invert Eq. (5) to obtain $\Theta(z,V_s)$, V_s was first converted to $V_s^\star$. If the resulting value was greater than 4.4, an initial value of Θ, Θ_i, was obtained using the first two terms on the right of Eq. (5)

$$\Theta_i = (V_s^\star - c)/m \qquad (10)$$

If $V_s^\star$ was less than 4.4, Θ_i was instead set to 1000 °C and Θ obtained from $V_s^\star$ using Newton–Raphson iteration. Less than five iterations were required for an accuracy of 0.1 °C.

The functional form of the parameterisation was chosen partly to allow comparison with constants determined from laboratory experiments. Jackson et al. [16] used their melt-free experiments to estimate a value of E of 390–400 kJ mol^{-1}, which is in good agreement with the value from geophysical observations. The value they obtained when melt was present was 520–540 kJ mol^{-1}. The agreement between the geophysical estimate of E and that from the melt-free, but not the melt-present, experiments supports the argument that the seismic low velocity zone beneath the Pacific results simply from the effect of temperature. The value of V_a, of 12 cm^3 mol^{-1}, used by Faul and Jackson [12] is not as well constrained as is that of E. Sato et al. [40] estimated V_a from high frequency measurements of Q, and obtained a value of 11 cm^3 mol^{-1} at 1 GPa, decreasing to 8 cm^3 mol^{-1} at 3 GPa. All these estimates are similar to that of 10 cm^3 mol^{-1} obtained
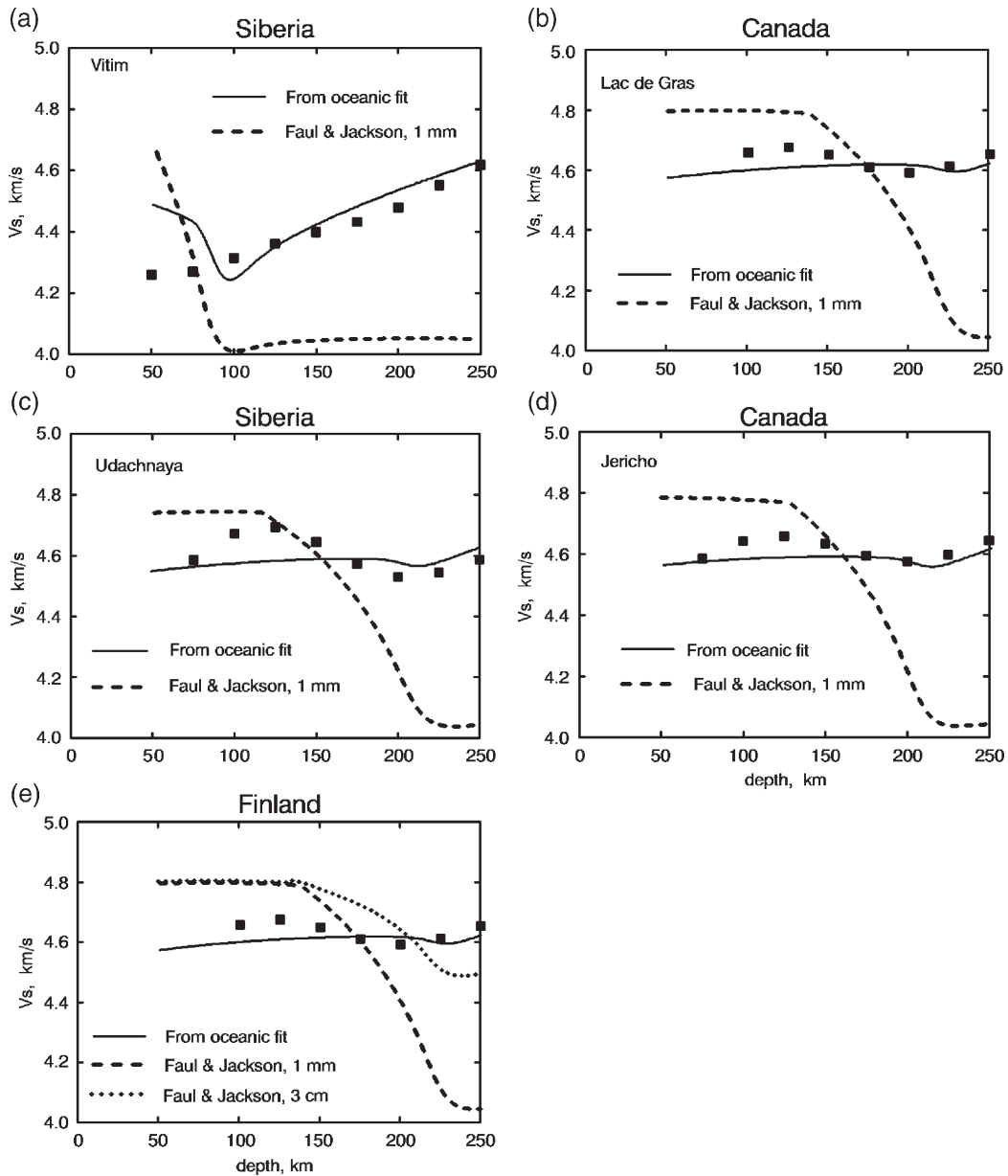
Fig. 6. Comparison of V_s profiles at the locations of the pipes (solid squares) with those calculated from the geotherms in Fig. 2 using Eq. (5) (solid lines) and with Faul and Jackson's [12] expressions with a grain size of 1 mm (dashed lines). The dotted line in (e) shows the corresponding curve for a grain size of 3 cm.

here. The value of A must depend on grain size and frequency, as well as on S_a, the entropy of the activation process, through a factor $\exp(S_a/R)$. The large value of A obtained from the geophysical observations suggests that the microscopic processes that cause the decrease in V_s at high temperatures involve large increases in entropy, as would be expected if they involve the formation of vacancies or interstitial atoms. The value of m can also be compared with laboratory measurements

of $(\partial V_s / \partial T)_P$ made at temperatures that are sufficiently low for the activated process to be unimportant, when m should be independent of frequency. Measurements of the shear modulus at a frequency of 30 MHz reported by Liu et al. [41] give a value of m for olivine at 800 °C of -3.75×10^{-4} km s^{-1} °C^{-1}, which is similar to, though slightly smaller than, the geophysical estimate of -2.8×10^{-4} km s^{-1} °C^{-1}. This difference may result from the limited vertical resolution of the surface waves,

or may be real and result from the difference in mineralogy between the laboratory experiments and the oceanic lithosphere. In particular, pyroxene compositions are strongly affected by the temperature of equilibration.

The conclusion that the observed decrease in V_s as the melting point is approached is due to temperature alone, and not due to the presence of melt, disagrees with the views of many previous authors. A particularly careful and detailed study of the lateral variation of V_s of the East Pacific Rise was carried out by Dunn and Forsyth [4] using Love waves recorded by ocean bottom seismometers. They found a difference in velocity of about 2% between the two flanks of the Rise. They argued that this behaviour cannot be due to temperature alone, because they estimated that the difference in velocity required a temperature difference of 350 °C. However, their argument assumed a linear relationship between velocity and temperature. The velocities at a depth of 60 km on the west and east side of the rise are approximately 4.1 and 4.2 km/s, respectively, a variation of 2.3%. The corresponding temperatures, calculated from Eq. (5), are 1346° and 1323°. This temperature difference, of 23 °C, is of similar magnitude to larger scale temperature variations below the Pacific lithosphere (see below). The observed velocity contrast therefore does not require the presence of melt.

4. Lithospheric thickness from V_s

The parameterisation outlined above can be used to test some of our ideas about the thermal structure of the continents and oceans in a number of ways. It is generally believed that the lithosphere forms a cold boundary layer to the convective system below, where variations in the potential temperature are small except in hot and cold thermal plumes. Fig. 7 shows the temperature at a depth of 150 km beneath the Pacific and at 250 km beneath eastern Asia, calculated from the shear wave velocity using Eq. (5). Except beneath the island arcs, the temperature beneath the Pacific is within 20 °C of 1400 °C throughout the entire region (Fig. 7a). The elevated temperatures beneath Hawaii are not visible because the lateral resolution is similar to the correlation length of 800 km, and the width of the Hawaiian plume is probably only about 100 km at a depth of 150 km. The small temperature variations that are visible in Fig. 7a correlate with plate age. Though they may be real, they could also be the result of the limited vertical resolution of the long period surface waves used for the tomography. However, even if the temperature variations in Fig. 7a are real, they are small. The plate model of the oceanic lithosphere that was used

to parameterise $V_s(z, \Theta)$ assumes that the temperature at the base of the lithosphere is constant. Fig. 7a shows that this assumption is a good approximation. In continental regions the lithospheric thickness is greater than it is beneath oceans. Fig. 7b shows the calculated temperature variations at a depth of 250 km, a depth which is probably greater than the lithospheric thickness almost everywhere. Though the temperature variations are slightly greater than those in Fig. 7a, they are largely unrelated to the crustal structure of the continent and to the continent–ocean boundaries. The only obvious exception is in the region of Tibet, where there is a large cool region at this depth.

An obvious extension of these arguments is to use the regional variations of $V_s(z)$ to map the lithospheric thickness. Fig. 8 compares the temperature profiles for the five locations in Fig. 2 calculated from the nodule mineralogy with those obtained from V_s using Eq. (5). The good agreement between the calculated and observed values is required by the parameterisation, and is not an independent test of its accuracy. The values of V_s obtained from surface wave tomography at depths of 100 km or less are not plotted. They are likely to be lowered by the low crustal velocities, because the vertical resolution of the tomographic inversion is between 25 and 50 km and the crustal thickness can exceed 60 km. This effect can artificially increase the temperatures at a depth of 75 km. The temperature estimates from V_s therefore increase in accuracy with increasing depth, as the influence of the crust decreases and the temperature increases. The small vertical arrows in Fig. 8c–e at a depth of 100 km show the change in temperature that would result if mantle, depleted by the removal of 25% melt, rather than fertile mantle, was used to calculate the temperature. The estimates of lithospheric thickness are listed in Table 1. The mean difference between the lithospheric thickness calculated from $\Theta(z, V_s)$ and that from Brey and Kohler's [31] expressions is 12 km, and that from Finnerty and Boyd's [30] is 0 km. Partly because of the nonlinear relationship between Θ and V_s, it is not straightforward to obtain accurate estimates of the lithospheric thickness from V_s. Eq. (5) shows that an uncertainty of 0.1 km/s in V_s corresponds to a temperature uncertainty of about 360 °C at low temperature, decreasing to 160 at 1200 °C, and to 37 °C. Temperature estimates from Faul and Jackson's expressions [12] are also show in Fig. 8.

These arguments show that only those temperature estimates from V_s that exceed 1100 °C at depths greater than 100 km are likely to be accurate, and only these were used to obtain the values of the lithospheric thickness contoured in Fig. 9. The estimates of
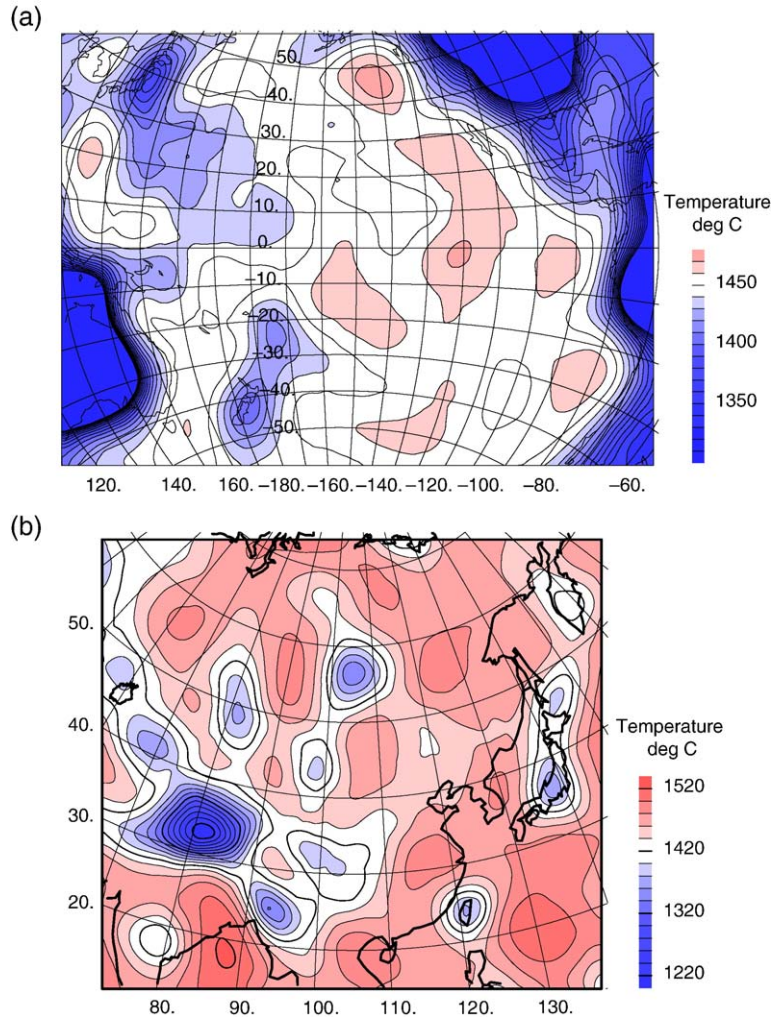
Fig. 7. (a) Temperature at a depth of 150 km beneath the Pacific Ocean, calculated from the shear wave velocity using Eq. (5) and contoured at 10 °C intervals. Because of the paths used, the temperatures are only well determined beneath the ocean basin. (b) As for (a) but for eastern Asia at a depth of 250 km and contoured at 20 °C intervals.

lithospheric thickness are largely controlled by the rapid decrease in V_s that occurs at high temperature, and the depth at which this decrease occurs is only well constrained if higher mode velocities, as well as that of the fundamental, are used to obtain $V_s(z)$. The thicknesses were obtained by first constructing vertical profiles of $V_s(z)$ for the continents at intervals of two degrees in latitude and longitude. Each value of V_s was then converted to a temperature using Eq. (5), and the temperature profile fitted to an individual geotherm using the approach of McKenzie et al. [32], assuming that the potential temperature was 1315 °C everywhere in the upper mantle. The lithospheric thickness was then calculated by extrapolating the conductive part of the geotherm until it intersected the isentropic profile for this potential temperature [32]. Because of the

restrictions on depth and temperature, the resulting values of lithospheric thickness are only likely to be accurate where they exceed about 120 km. The estimated thickness of the Canadian lithosphere is about 100 km thinner than that of Shapiro et al. [17], probably because they only used fundamental mode group and phase velocities. Fig. 9 shows contour maps of lithospheric thickness for Africa and Eurasia, together with a number of point estimates from nodule mineralogy (Table 1) and the locations of diamond-bearing kimberlites [42]. Since most diamonds are lithospheric xenocrysts, the locations of such kimberlites provide an independent test for the presence of lithosphere that is thicker than about 140 km. The spatial variations are surprisingly rapid in some places. The values of lithospheric thickness from east African nodules increase
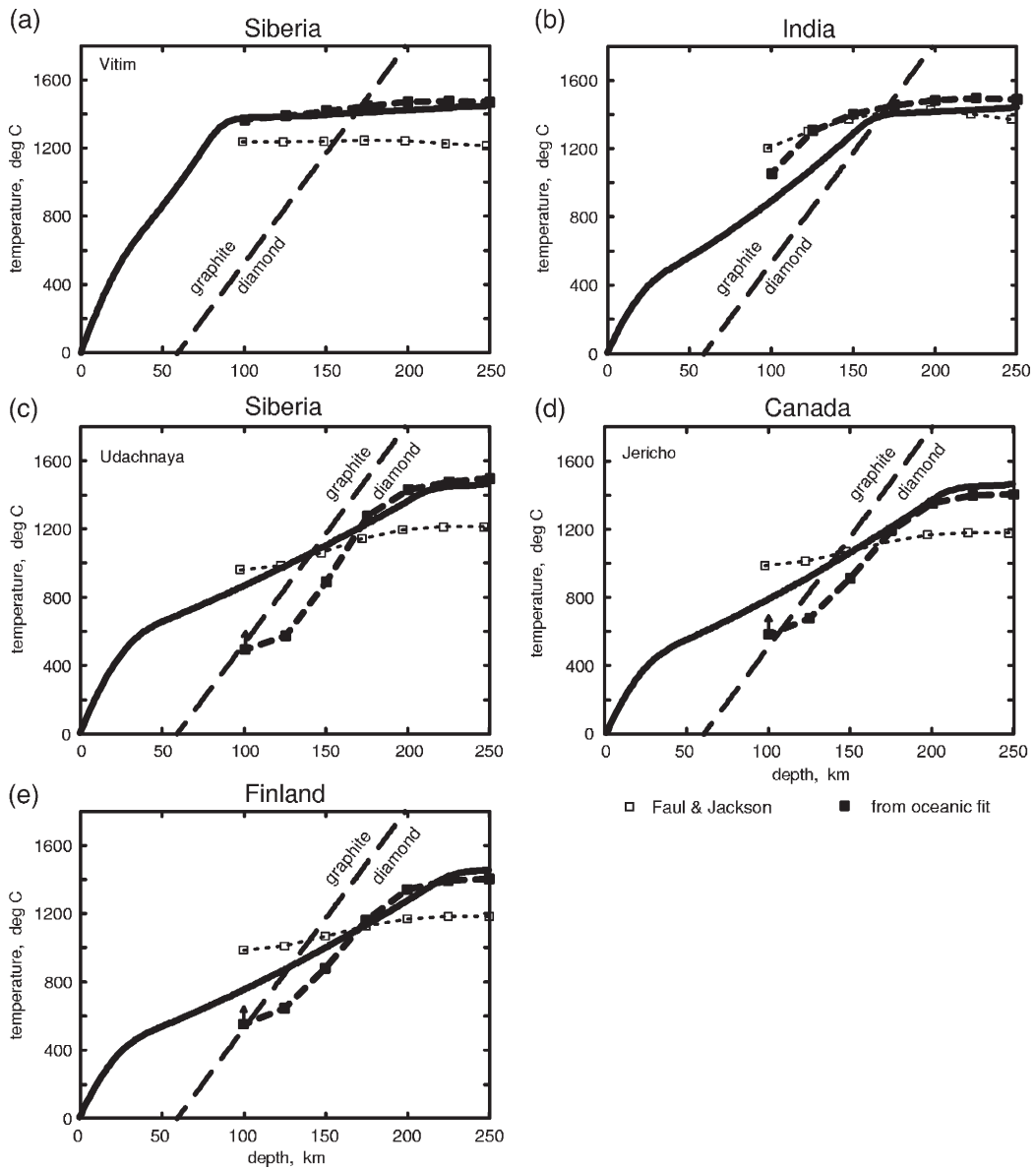
Fig. 8. Comparison of temperatures, calculated from the shear wave velocities, with the geotherms from the nodule mineralogies for the five pipes shown in Fig. 2. The corresponding lithospheric thicknesses are given in Table 1. The solid squares show the temperature estimates from Eq. (5), and the open squares those obtained from Faul and Jackson's [12] expressions. The small vertical arrows at depths of 100 km in (c), (d) and (e) show the increase in the calculated temperature that would result if the mantle at this depth had been depleted by the removal of 25% melt.

from 88 to 143 km (Fig. 9a) in a distance of about 350 km, where that calculated from V_s also shows a rapid increase. Furthermore the largest diamond mine in the world, at Mwadui in Tanzania, probably has a lithospheric thickness of 200–250 km. This increase is therefore real. A similar increase occurs in eastern Siberia (Fig. 9b). In both places the changes in lithospheric thickness are probably too rapid to be accurately resolved by the long period surface waves used to obtain $V_s(z)$.

Figs. 9 and 10 show that many, but not all, of the cratons are underlain by thick lithosphere. However the regions of thick lithosphere are often more extensive and continuous than are the cratons. For instance the Angolan, Tanzanian and Kalahari Cratons (b, c and d in Fig. 9a) are underlain by a single continuous region of thick lithosphere. Similarly the East European and Siberian Cratons (a and b in Fig. 9b) are both underlain by one region of thick lithosphere that extends under the Urals and the West Siberian Basin which lie
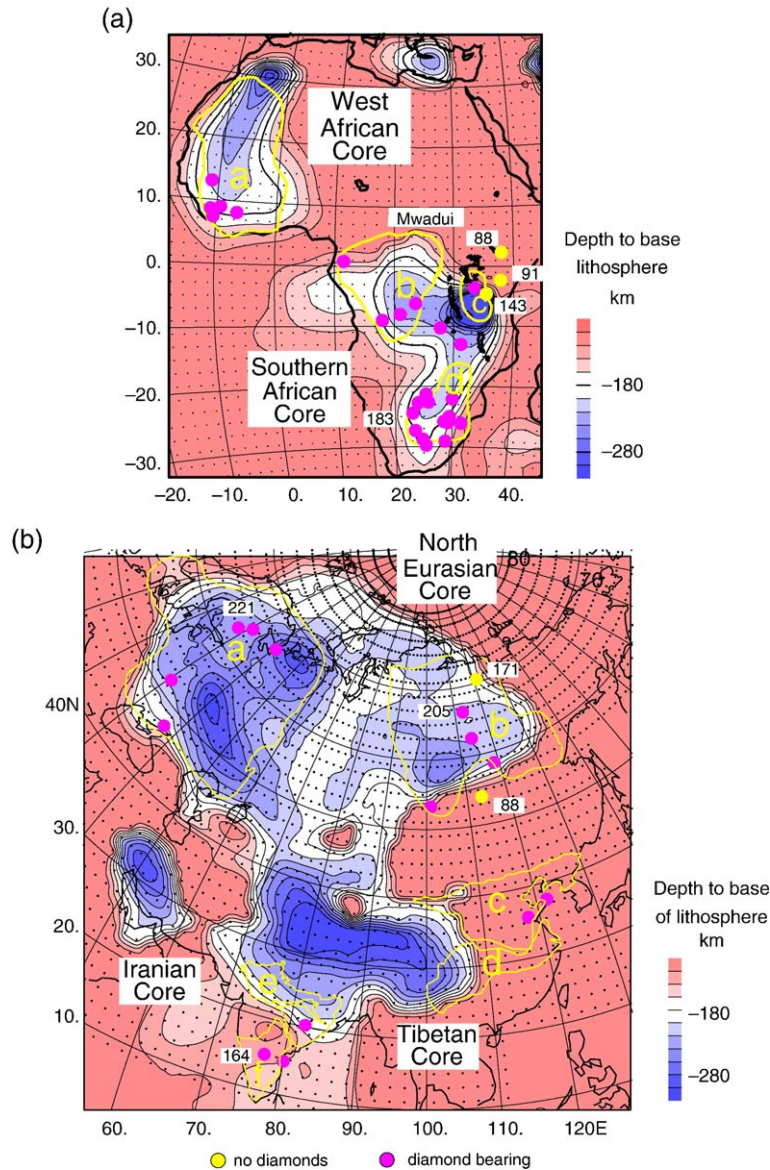
Fig. 9. Regional variations in lithospheric thickness, calculated by converting $V_s(z)$ into $\Theta(z)$ and then fitting geotherms [32] (see text). The small dots, at intervals of 2°, show the locations at which the thickness was estimated. The yellow circles show locations of diamond-free kimberlites and alkali basalts where the lithospheric thickness, shown in the white boxes, has been estimated from the nodule mineralogies. The red dots show the locations of diamond-bearing kimberlites, marked with the value of lithospheric thickness where this has been estimated. The yellow lines outline the approximate boundaries of cratons. In (a) these are (a) West African Craton, (b) Angolan Craton, (c) Tanzanian Craton, (d) Kalahari Craton, and in (b) (a) East European Craton, (b) Siberian Craton, (c) North China Craton, (d) Yangtze Block of the South China Craton, (e) Bastar, Singhbhum, and Arivalli Cratons, and (f) Dharwar Craton.

between them. Though the limited spatial resolution of the surface waves cannot resolve gaps between cratons that are less than about 400 km, this effect cannot account for the lithospheric thickness beneath the West Siberian Basin, or that beneath the interior lowlands in Fig. 10b. However some cratons, such as the North China Craton and the Dhawar Craton of southern India (Fig. 9b, c and f), are not now underlain by thick

lithosphere, though the occurrence of diamond-bearing kimberlites in both regions suggest that it was once present. Partly because of the limited correspondence between cratons and regions of thick lithosphere, and partly because seismology provides no age control, we prefer to refer to continuous regions of thick lithosphere as 'cores' rather than as cratons, and have named those in Figs. 9 and 10 that are well resolved.
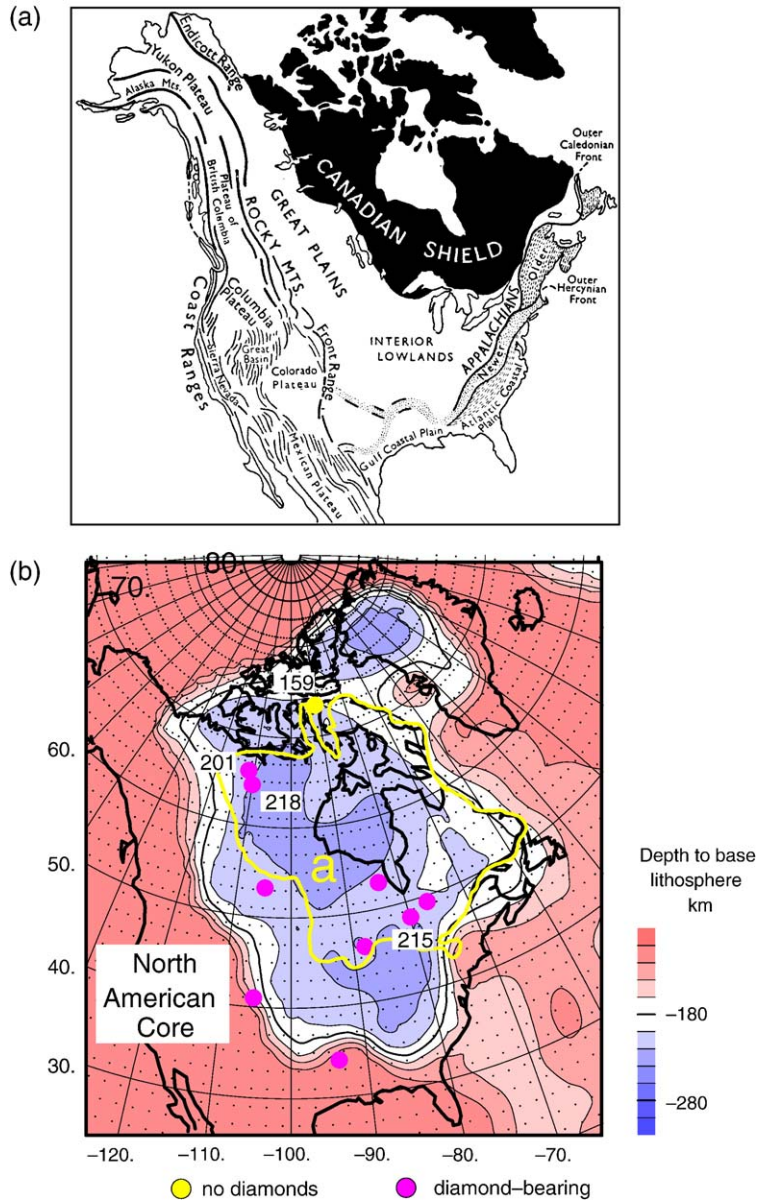
Fig. 10. (a) Tectonic map of North America [56, Fig. 811]. (b) As for Fig. 9, the yellow line shows the approximate margin of the North American Craton.

The tectonics of Eurasia, and especially that of North America, is largely controlled by the shape of their cores. Fig. 10a shows that the Rocky Mountains and the Appalachians wrap around the margins of the North American Core.

The most surprising feature of the maps in Figs. 9 and 10 is the existence of thick lithosphere beneath Iran and Tibet. The corresponding values of V_s are well resolved (see Fig. 7) and all of the structures in Fig. 9b were determined using the same seismograms. There is therefore no reason to suspect that the thick lithosphere

in these regions is an artifact. The velocity structure beneath Tibet is similar to that of other regions of thick lithosphere, except that it is displaced downwards by about 50 km by the thicker crust.

5. Conclusions

Laboratory measurements of the shear modulus of polycrystalline olivine at frequencies of $1-10^{-2}$ Hz show that it decreases strongly with increasing temperature at temperatures that are considerably below the

macroscopic solidus [9,16]. These experiments also show that the behaviour is strongly affected by the grain size, which is usually several orders of magnitude smaller in the laboratory experiments than it is in the mantle. Gribb and Cooper [9] suggested that this velocity decrease was the result of grain boundary diffusion, but did not obtain an expression for $V_s(\Theta)$. Faul and Jackson [12] used a complicated expression to do so, based partly on the assumption that Q is constant, which they then applied to the geophysical observations.

The laboratory experiments of both groups do not support the common belief among geophysicists that the low shear wave velocities beneath spreading ridges and in the low velocity zone beneath the plates result from the presence of a macroscopic melt phase. Since the thermal structure of oceanic lithosphere is now well constrained, V_s from surface wave tomography can be used to test the accuracy of Faul and Jackson's [12] expressions. These do not agree well with the geophysical observations unless the grain size increases with depth by more than an order of magnitude. However, the grain size is expected to decrease, not increase, with increasing depth, as the rate of shearing and the fertility of the mantle increase. Nodules from kimberlite pipes also show that the grain size decreases with increasing depth of origin [33]. We therefore took a simple empirical approach, and used the geophysical observations themselves to parameterise $V_s(z,\Theta)$. Our parameterisation contains a number of adjustable constants whose values we determined from the V_s observations, but does not explicitly depend on grain size or frequency. Two of the constants which control the high temperature behaviour are the activation energy, of $E=409$ kJ/mol, and activation volume, of $V_a=10$ cm^3/mol. The value of E agrees well with the estimate of Jackson et al. [16], of 390–400 kJ/mol, from laboratory experiments in the absence of melt. We then used the empirical expression to calculate the regional variations of lithospheric thickness, and compared the resulting maps with the distribution of diamond-bearing kimberlites. The thicknesses obtained in this way are likely to be accurate to about ± 20 km, because the temperature resolution is good near the base of thick lithosphere where the temperature is high, and therefore $|\partial V_s / \partial z|$ is large, and the values of V_s from tomography are unaffected by the crust. In most places diamond-bearing kimberlites only occur where the lower part of the lithosphere is now in the diamond stability field. However, the lithosphere is now thin beneath the Ordovician diamondiferous kimberlites of NE China, perhaps because of stretching. Proterozoic diamond-bearing kimberlites of the Indian Peninsula are also now underlain by thin lithosphere.

Acknowledgements

References

[1] B. Gutenberg, Physics of the Earth's Interior, Academic Press, New York, 1959.

[2] D.L. Anderson, C.G. Sammis, Partial melting in the upper mantle, Phys. Earth Planet. Int. 3 (1970) 41–50.

[3] W.C. Hammond, E.D. Humphreys, Upper mantle seismic wave velocity: effects of realistic partial melt geometries, J. Geophys. Res. 105 (2000) 10975–10986.

[4] R.A. Dunn, D.W. Forsyth, Imaging the transition between the region of melt generation and crustal magma chamber beneath the southern East Pacific Rise with short-period Love waves, J. Geophys. Res. 108 (B7) (2003), doi:10.1029/2002JB002217.

[5] S. Karato, Importance of anelasticity in the interpretation of seismic tomography, Geophys. Res. Letts. 20 (1993) 1623–1626.

[6] D. McKenzie, ^{230}Th–^{238}U disequilibrium and the melting processes beneath ridge axes, Earth Planet. Sci. Lett. 72 (1985) 149–157.

[7] A. Stracke, A. Zindler, V.J.M. Salters, D. McKenzie, K. Gronvold. The dynamics of melting beneath Iceland. G^3 4 (2003) (10) 18 pp., 8513, doi:10.1029/2002GC000347.

[8] T.T. Gribb, R.F. Cooper, The effect of an equilibrated melt phase on the shear creep and attenuation behaviour of polycrystalline olivine, Geophys. Res. Letts. 27 (2000) 2341–2344.

[9] T.T. Gribb, R.F. Cooper, Low-frequency shear wave attenuation in polycrystalline olivine: grain boundary diffusion and the physical significance of the Andrade model for viscoelastic rheology, J. Geophys. Res. 103 (1998) 27267–27279.

[10] I. Jackson, Laboratory measurements of seismic wave dispersion and attenuation: recent progress, The Earth's deep interior: mantle physics and tomography from atomic to the global scale, Geophysical Monograph, American Geophysical Union, vol. 117, 2000, pp. 265–289.

[11] K. Priestley, D. McKenzie, The structure of the upper mantle beneath southern Africa, in: C.M.R. Fowler, C.J. Ebinger, C.J. Hawkesworth (Eds.), The Early Earth: Physical, Chemical and Biological Development, Geol. Soc. Lond. Special Publ., vol. 199, 2002, pp. 45–64.

[12] U.H. Faul, I. Jackson, The seismological signature of temperature and grain size variations in the upper mantle, Earth Planet. Sci. Lett. 234 (2005) 119–134.

[13] H. Kanamori, D.L. Anderson, Importance of physical dispersion in surface wave and free oscillation problems, Rev. Geophys. Space Phys. 15 (1977) 105–112.

[14] D.L. Anderson, J.B. Minster, The frequency dependence of Q in the Earth and implications for mantle rheology and the Chandler wobble, Geophys. J. Roy. Astron. Soc. 58 (1979) 431–440.

[15] F.A. Dahlen, J. Tromp, Theoretical Global Seismology, Princeton University Press, Princeton NJ, 1998.

[16] I. Jackson, J.D. FitzGerald, U.H. Faul, B.H. Tan, Grain-size sensitive seismic wave attenuation in polycrystalline olivine, J. Geophys. Res. 107 (B12) (2002), doi:10.1029/2001JB001225.

[17] N.M. Shapiro, M.H. Ritzwoller, J.C. Mareschal, C. Jaupart, Lithospheric structure of the Canadian Shield inferred from inversion of surface-wave dispersion with thermodynamic a priori constraints, in: A. Curtis, R. Wood (Eds.), Geological Prior Information: Informing Science and Engineering, Geol. Soc. London Spec. Publ., vol. 239, 2004, pp. 175–194.

[18] E. Debayle, B.L.N. Kennett, The Australian continental upper mantle: structure and deformation inferred from surface waves, J. Geophys. Res. 105 (2000) 25423–25450.

[19] K. Priestley, E. Debayle, Seismic evidence for a moderately thick lithosphere beneath the Siberian Platform, Geophys. Res. Letts. 30 (2003), doi:10.1029/2002GL015931.

[20] E. Debayle, SV-wave azimuthal anisotropy in the Australian upper mantle: preliminary results from automated Rayleigh waveform inversion, Geophys. J. Int. 137 (1999) 747–754.

[21] M. Cara, J.J. Lévêque, Waveform inversion using secondary observables, Geophys. Res. Letts. 14 (1987) 1046–1049.

[22] J.P. Montagner, Regional three-dimensional structures using long-period surface waves, Ann. Geophys. 4 (1986) 283–294.

[23] E. Debayle, M. Sambridge, Continuous regionalization of massive surface wave data sets: model construction and resolution assessment J. Geophys. Res. 109 (2004), doi:10.1029/2003JB002652.

[24] J.H. Woodhouse, Surface waves in a laterally varying layered structure, Geophys. J. Roy. Astron. Soc. 37 (1974) 461–490.

[25] B.L.N. Kennett, Approximations for surface-wave propagation in laterally varying media, Geophys. J. Int. 122 (1995) 470–478.

[26] M.H. Ritzwoller, N.M. Shapiro, M.P. Barmin, A.L. Levshin, Global surface wave diffraction tomography, J. Geophys. Res. 107 (2002), doi:10.1029/2002JB001777.

[27] H. Marquering, R. Snieder, G. Nolet, Waveform inversion the significance of surface-wave mode coupling, Geophys. J. Int. 124 (1996) 258–278.

[28] A. Sieminski, J.J. Lévêque, E. Debayle, Can finite-frequency effects be accounted for in ray theory surface wave tomography? Geophys. Res. Letts. 31 (2004) 31, doi:10.1029/2004GL021402.

[29] R.D. Mueller, W.R. Roest, J.-Y. Royer, L.M. Gahagan, J.G. Sclater, A digital age map of the ocean floor, J. Geophys. Res. 102 (1997) 3211–3214.

[30] A.A. Finnerty, F.R. Boyd, Thermobarometry for garnet peridotites: and compositional structure of the upper mantle, in: P.H. Nixon (Ed.), Mantle Xenoliths, J. Wiley & Sons, New York, 1987, pp. 381–402.

[31] G.P. Brey, T. Kohler, Geothermobarometry in four-phase lherzolites: II. New thermobarometers, and practical assessment of existing thermobarometers, J. Petrol. 31 (1990) 1353–1378.

[32] D. McKenzie, J. Jackson, K. Priestley, Thermal structure of oceanic and continental lithosphere, Earth Planet Sci. Lett. 233 (2005) 337–349.

[33] B. Harte Mantle peridotites and processes—the kimberlite sample, in: C.J. Hawkesworth, M.J. (Eds.), Continental Basalts and Mantle Xenoliths, Norry Shiva Publishing Ltd, Cheshire U. K. pp. 46–91.

[34] D. McKenzie, R.K. O'Nions, Partial melt distributions from inversion of rare earth element concentrations, J. Petrol. 32 (1991) 1021–1091 (correction 33(1992) 1453).

[35] D. McKenzie, M.J. Bickle, The volume and composition of melt generated by extension of the lithosphere, J. Petrol. 29 (1988) 625–679.

[36] X. Qiu, K. Priestley, D. McKenzie, Average lithospheric structure of southern Africa, Geophys. J. Int. 127 (1996) 563–587.

[37] T.H. Jordan, Mineralogies, densities and seismic velocities of garnet lherzolites and their geophysical implications, in: F.R. Boyd, H.O.A. Meyer (Eds.), The Mantle Sample: Inclusions in Kimberlites and Other Volcanics, Proc. 2nd International Kimberlite Conference, vol. 2, American Geophysical Union, 1979, pp. 1–14.

[38] S. Goes, R. Govers, P. Vacher, Shallow mantle temperatures under Europe from P and S wave tomography, J. Geophys. Res. 105 (2000) 11,153–11,169.

[39] N.M. Shapiro, M.H. Ritzwoller, Thermodynamic constraints on seismic inversions, Geophys. J. Int. 157 (2004) 1175–1188.

[40] H. Sato, I.S. Sacks, T. Murase, G. Muncill, H. Fukuyama, Qp-melting temperature relation in peridotite at high pressure and temperature: attenuation mechanism and implications for the mechanical properties of the upper mantle, J. Geophys. Res. 94 (1989) 10647–10661.

[41] W. Liu, J. King, B. Li, Elasticity of San Carlos olivine to 8 GPa and 1073 K, Geophys. Res. Letts. 32 (2005), doi:10.1029/2005GL02JI 3453 (L16301).

[42] A.J.A. Janse, P.A. Sheahan, Catalogue of world wide diamond and kimberlite occurrences: a selective and annotative approach, J. Geochem. Explor. 53 (1995) 73–111.

[43] D. Zhao, E.J. Essene, Y. Zhang, C.M. Hal, L. Wang Newly discovered kimberlites and mantle xenoliths from Somerset Island and Brodeur Peninsula, Canada: Pressure, temperature and oxygen fugacity, volatile content and age. NWT Geology Division, Dept. of Indian and Northern Affairs, Yellowknife. EGS open file 1997-5.

[44] S.S. Schmidberger, D. Francis, Nature of mantle roots beneath the North American craton: mantle xenolith evidence from Somerset Island kimberlites, Lithos 48 (1999) 195–216.

[45] M.G. Kopylova, J.K. Russell, H. Cookenboo, Petrology of peridotite and pyroxenite xenoliths from the Jericho kimberlite: implications for thermal state of the mantle beneath the Slave craton northern Canada, J. Petrol. 40 (1998) 79–104.

[46] N.J. Pearson, W.L. Griffin, B.J. Doyle, S.Y. O'Reilly, E. van Achterbergh, K. Kiwi, Xenoliths from kimberlite pipes of the Lac de Gras area, Slave craton, Canada, in: J.J. Gurney, J.T. Gurney, M.D. Pascoe, S.H. Richardson (Eds.), Int. Kimberlite Conference, vol. 7, 1999, pp. 644–658.

[47] H.O.A. Meyer, M.A. Waldman, B.L. Garwood, Mantle xenoliths from kimberlite near Kirkland Lake, Ontario, Can. Mineral. 32 (1994) 295–306.

[48] I.T. Kukkonen, P. Peltonen, Xenolith-controlled geotherm for the central Fennoscandian Shield: implications for litho-sphere–asthenosphere relations, Tectonophys. 304 (1999) 301–315.

[49] F.R. Boyd, N.P. Pokhilenko, D.G. Pearson, S.A. Mertzman, N.V. Sobolev, L.W. Finger, Composition of the Siberian cratonic mantle: evidence from Udachnaya peri-dotite xenoliths, Contrib. Mineral. Petrol. 128 (1997) 228–246.

[50] L.A. Taylor, G.A. Snyder, R. Keller, D.A. Remley, M. Anand, R. Wiesli, J. Valley, N.V. Sobolev, Petrogenesis of group A eclogites and websterites: evidence from Obnazhennaya kimberlite, Yakutia, Contrib. Mineral. Petrol. 145 (2003) 424–443.

[51] D.A. Ionov, I.V. Ashchepkov, H.-G. Stosch, G. Witt-Eickschen, H.A. Seck, Garnet peridotite xenoliths from the Vitim volcanic field, Baikal region: the nature of the garnet-spinel peridotite transition zone in the continental mantle, J. Petrol. 34 (1993) 1141–1175.

[52] J. Ganguly, P.K. Bhattacharya, Xenoliths in Proterozoic kimberlites from southern India: petrology and geophysical

implications, in: P.H. Nixon (Ed.), Mantle Xenoliths, J. Wiley & Sons, New York, 1987, pp. 249–265.

[53] F. Henjes-Kunst, R. Alterr, Metamorphic petrology of xenoliths from Kenya and northern Tanzania and implications for geotherms and lithospheric structure, J. Petrol. 33 (1992) 1125–1156.

[54] C.-T. Lee, R.L. Rudnick, Compositionally stratified cratonic lithosphere: petrology and geochemistry of peridotite xenoliths from the Labiat Volcano, Tanzania, in: J.J. Gurney, J.T. Gurney, M.D. Pascoe, S.H. Richardson (Eds.), Int. Kimberlite Conference, vol. 7, 1999, pp. 503–521.

[55] C.S. Kennedy, G.C. Kennedy, The equilibrium boundary between graphite and diamond, J. Geophys. Res. 81 (1976) 2467–2470.

[56] A. Holmes, The Principles of Physical Geology, Nelson Edinburgh, 1965.